

Holographic detection of parity in atomic and molecular orbitalsHuiPeng Kang^{1,2,*}, Andrew S. Maxwell,³ Daniel Trabert,¹ XuanYang Lai,² Sebastian Eckart,¹ Maksim Kunitski,¹ Markus Schöffler,¹ Till Jahnke,¹ XueBin Bian², Reinhard Dörner,¹ and Carla Figueira de Morisson Faria³¹*Institut für Kernphysik, Goethe Universität Frankfurt, 60438 Frankfurt am Main, Germany*²*State Key Laboratory of Magnetic Resonance and Atomic and Molecular Physics, Wuhan Institute of Physics and Mathematics, Innovation Academy for Precision Measurement Science and Technology, Chinese Academy of Sciences, Wuhan 430071, China*³*Department of Physics and Astronomy, University College London, Gower Street, London WC1E 6BT, United Kingdom*

(Received 6 August 2019; revised 1 March 2020; accepted 24 June 2020; published 20 July 2020)

We introduce a concise methodology to detect the parity of atomic and molecular orbitals based on photoelectron holography, which is more general than the existing schemes. It fully accounts for the Coulomb distortions of electron trajectories, does not require sculpted fields to retrieve phase information and, in principle, is applicable to a broad range of electron momenta. By comparatively measuring the differential photoelectron spectra from strong-field ionization of N_2 molecules and their companion atoms of Ar, some photoelectron holography patterns are found to be dephased for both targets. This is well reproduced by the full-dimensional time-dependent Schrödinger equation and the Coulomb quantum-orbit strong-field approximation (CQSFA) simulation. Using the CQSFA, we trace back our observations to different parities of the $3p$ orbital of Ar and the highest-occupied molecular orbital of N_2 via interfering Coulomb-distorted quantum orbits carrying different initial phases. This method could in principle be used to extract bound-state phases from any holographic structure, with a wide range of potential applications in recollision physics and spectroscopy.

DOI: [10.1103/PhysRevA.102.013109](https://doi.org/10.1103/PhysRevA.102.013109)**I. INTRODUCTION**

Parity is of fundamental importance in many areas of physics, e.g., atomic and molecular physics, cosmology, and particle physics. It is conserved in electromagnetism, strong interactions, and gravity, but not in weak interactions [1]. In quantum mechanics, it mostly relates to the symmetry of wave functions representing microscopic particles, and to quantum phase differences. For an atom or molecule interacting with a strong laser field, the parity of electronic orbitals governs many phenomena such as resonant multiphoton transitions [2], molecular ionization suppression [3], and the phase differences acquired by the tunneling wave packet [4–7].

In the context of above-threshold ionization (ATI), schemes to detect parity using quantum interference have been proposed. For instance, one may use sculpted fields [8], where Coulomb effects have been approximated by a simple eikonal phase, or interference carpets, whose explanation ignores the residual Coulomb potential [9]. However, Coulomb distortion represents a troublesome issue for directly probing parity, as it modifies the interfering trajectories themselves [10–12]. This includes the number of trajectories, their shapes, initial momenta, and ionization times. Thus, it is questionable whether additional phase shifts around Coulomb-free orbits will lead to a reliable modeling of the system's dynamics. A way around this is to consider momentum ranges for which the Coulomb potential is not crucial and adopt highly directional

methods. For instance, in [9] scattering angles perpendicular to the driving-field polarization, for which Coulomb effects cancel out, were used. Furthermore, in [8] only a small portion of photoelectrons with low perpendicular and high parallel momenta with respect to laser polarization are suitable for inferring the parity information. This limits the applicability of such methods, and may be problematic for larger systems such as polyatomic molecules, which may be difficult to align. It is also noteworthy that, even for simple molecules, the detection of parity for molecular systems remains elusive. In this paper, we introduce a general and concise differential holographic method which deals with above issues.

Ultrafast photoelectron holography [13,14] is a very powerful imaging technique based on the physical picture of laser-driven recollision [15] which combines high electron currents with subfemtosecond time resolution. Thereby, a probe and a reference wave are employed to reconstruct a target by recording phase differences between them. Both probe and reference terms stem from qualitatively different ionization pathways, which can be associated with interfering electron wave packets. This phase encoding makes it an ideal tool to probe the parity of the atomic and molecular orbitals (for a review see [14]).

Since its inception, ultrafast photoelectron holography has been used for extracting not only structural information [16], but also for visualizing the attosecond dynamics of valence electron motion [17] and revealing the coupled electronic and nuclear dynamics of molecules [18]. Prominent holographic examples are the spiderlike [13], the carpetlike [9], and the near-threshold fan-shaped structures [19–21]. The spider and in particular the fan are caused by the interplay between the residual Coulomb potential and the laser field [22–24].

*Present address: Institute of Optics and Quantum Electronics, Friedrich Schiller University Jena, Max-Wien-Platz 1 and Helmholtz Institut Jena, Fröbelstieg 3, 07743 Jena, Germany; H.Kang@gsi.de

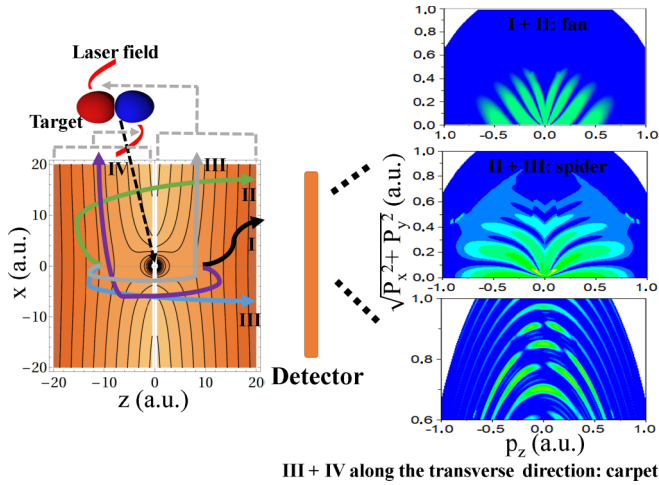


FIG. 1. Schematic representation of dominant trajectories (left-hand side), classified from I to IV according to [10,25], contributing to characteristic interference patterns in the final photoelectron momentum distributions (right-hand side). The lower panel on the left side indicates the contour lines of laser-distorted potentials for an Ar atom at two adjacent laser field peaks. The laser peak intensity is chosen as 6.5×10^{13} W/cm² here. The interferences between types I and II (II and III) trajectories are responsible for the fan-shaped (spiderlike) structures [11,27,28]. The carpetlike structures result from the interferences between type-III and type-IV trajectories along the transverse direction [12]. Within the CQSFA theory, trajectories that pass closer than the tunnel exit can be considered as soft or hard rescattering, where hard rescattering trajectories pass within the Bohr radius, while soft rescattering trajectories do not. Trajectories of type III and IV are always rescattering ones here [12].

Recently, an orbit-based approach that incorporates the Coulomb potential and the laser field on equal footing, the Coulomb quantum-orbit strong-field approximation (CQSFA) [10], has offered a transparent picture of different interference structures. It also predicted a spiral-like holographic structure [12], whose high-energy limit gives the interference carpets in [9].

Here we demonstrate, both experimentally and theoretically, that photoelectron holography is a sensitive tool for probing the parity of atomic and molecular orbitals. We introduce a differential holographic method using an atom with comparable Coulomb effects to retrieve the parity of molecular orbital. Our article is organized as follows. In Sec. II, we outline the strategy to be followed and briefly discuss its experimental realization. In Sec. III we provide the theoretical background necessary to model and interpret our results. These are presented and discussed in Sec. IV. Finally, in Sec. V we state our conclusions. Information of either complementary or technical nature is provided in the Appendix.

II. STRATEGY AND EXPERIMENTAL SETUP

Our basic strategy is illustrated in Fig. 1. Let us consider an atomic or molecular orbital of odd parity. When irradiated by an intense laser pulse, the tunnel ionized electrons ending up with same final momentum lead to various interference patterns in the photoelectron momentum distribution. Within

TABLE I. Summary of the phase shifts expected for different types of orbits and initial bound states of different parity.

Structure	Orbits	Parity	Shift
Fan	I, II	even/odd	$0/\pi$
Spider	II, III	even/odd	$0/0$
Carpet	III, IV	even/odd	$0/\pi$

the CQSFA [10], each trajectory carries a phase that can be separated into two parts, i.e., the initial phase which includes the parity of the atomic or molecular orbital and the phase accumulated along the pathway from the origin until the detector. For each given final momentum, the electron trajectories can be distinguished into four groups, as introduced in CQSFA [10] or trajectory-based Coulomb-strong-field approximation theory [25]. For type-I trajectories, the electron moves directly to the detector without revisiting its parent core. For type-II and type-III trajectories, the electron first moves away from the detector and then turns around and finally arrives at the detector. For type-IV trajectories, the electron initially moving to the detector goes around the core and then again moves towards the detector. Ignoring the subcycle distortion of the orbital by the laser field, one can expect a shift of π between the initial phase of type-I and type-II (also type-III and type-IV) trajectories for an orbital with odd parity since they come from two opposite sides of the target, while there will be no such phase shift for an orbital with even parity. For the spiderlike structures, there will always be no initial phase shift irrespective of the orbital parity, because type-II and type-III trajectories are released on the same side. A summary is provided in Table I.

To experimentally realize the strategy, we use Ar as a reference atom to reveal information about the target molecule N₂. One important reason for this target choice is that the ground state $3p$ of Ar and the highest-occupied molecular orbital (HOMO) of N₂ have odd and even parities, respectively. Additionally, according to the CQSFA theory [10,11], for each type of trajectory in identical laser fields, the phase obtained along the continuum propagation is expected to be nearly identical for Ar and N₂ due to their close ionization potentials and similar long-range Coulomb effects, as we will see below. The initial phase encoding the parity of the atomic or molecular orbital is thus accessed by comparing the holographic patterns of the two targets. We find that the measured fan-shaped (and carpetlike) patterns show out of phase features for Ar and N₂, whereas the spiderlike patterns are in phase under identical laser conditions, which is in contrast with previous differential measurements [26]. The observations are reproduced by a numerical solution of the time-dependent Schrödinger equation (TDSE), as well as the CQSFA simulation. In terms of the CQSFA theory, we demonstrate that our findings can be ascribed to the different parities of the $3p$ orbital of Ar and the HOMO of N₂. This also defies the previous narrative that strong-field ionization of N₂ behaves like Ar and thus sheds light on the topic.

In our experiments, intense laser pulses at a central wavelength of 788 nm were generated by a commercial Ti:sapphire femtosecond laser system (100 kHz, 100 μ J, 45 fs, Wyvern-

500, KMLabs). The laser beam was then focused by a spherical concave mirror ($f = 60$ mm) onto a cold supersonic jet of mixture of Ar and N₂ inside the main chamber of a cold target recoil ion momentum spectroscopy (COLTRIMS) reaction microscope [29]. The use of a mixture gas jet substantially reduces the systematic uncertainties resulting from the absolute determination of each gas target density as well as the laser intensity, and beam pointing fluctuations during long-time measurements. The laser intensity in the interaction region was calibrated by measuring the “donut”-shape momentum distribution of singly charged Ne⁺ ions with circularly polarized light [30]. We did not align the N₂ molecules throughout our measurements.

We employed the COLTRIMS setup to simultaneously measure the three-dimensional momentum distributions of the electrons and ions from ionization of Ar and N₂. The photoelectrons and photoions were guided by homogeneous electric (27.6 V/cm) and magnetic (9.5 G) fields towards two microchannel plate detectors equipped with delay-line anodes [31] in order to obtain the positions of impinging particles. The spectrometer consisted of an ion arm with a 18.2 cm acceleration region and a 40.0 cm drift region, and an electron arm with an acceleration region of 7.8 cm. By checking for momentum conservation between the detected electrons and the singly charged ions, the events arising from false coincidences were suppressed substantially.

III. THEORY

A. Time-dependent Schrödinger equation

In the resent study, the TDSE was solved in the velocity gauge. We employed a cosine square function to represent the temporal profile of the laser pulse. The details about the TDSE simulations can be found elsewhere [32,33]. For Ar, the simulation was performed within the single-active-electron approximation for an effective model potential $V(r) = -(1 + a_1 e^{-a_2 r} + a_3 r e^{-a_4 r} + a_5 e^{-a_6 r})/r$ with $a_1 = 16.039$, $a_2 = 2.007$, $a_3 = -25.543$, $a_4 = 4.525$, $a_5 = 0.961$, and $a_6 = 0.443$ [34] considering a $3p$ ($m = 0$) orbital neglecting spin orbit interaction. For N₂ we only considered the HOMO in the simulation, and used the linear combination of atomic orbitals (LCAO) approximation [35]. This is reasonable as the sharp fringes in the experimental interference carpets suggest a single dominant orbital.

B. Coulomb quantum-orbit strong field approximation

The CQSFA theory describes ionization in terms of quantum orbits from the saddle-point evaluation of the Coulomb-distorted transition amplitude. In an exact form, the ionization amplitude reads

$$M(\mathbf{p}_f) = -i \lim_{t \rightarrow \infty} \int_{-\infty}^t dt_0 \langle \psi_{\mathbf{p}_f}(t) | \hat{U}(t, t_0) \hat{H}_I(t_0) | \psi_0(t_0) \rangle, \quad (1)$$

where $|\psi_0(t_0)\rangle = e^{iI_p t_0} |\psi_0\rangle$ is the initial bound state (I_p is the ionization potential) and the final state $|\psi_{\mathbf{p}_f}(t)\rangle$ is a continuum state with momentum \mathbf{p}_f . $\hat{U}(t, t_0)$ is the time-evolution operator of the Hamiltonian $\hat{H}(t) = \hat{\mathbf{p}}^2/2 + V(\hat{\mathbf{r}}) + \hat{H}_I(t)$, with $\hat{H}_I(t) = -\hat{\mathbf{r}} \cdot \mathbf{E}(t)$ and the Coulomb potential $V(\hat{\mathbf{r}})$. Using the

Feynman path-integral formalism [36,37] and the saddle-point approximation [38,39], Eq. (1) can be rewritten as [10,11]

$$M(\mathbf{p}_f) \propto -i \lim_{t \rightarrow \infty} \sum_s \left\{ \det \left[\frac{\partial \mathbf{p}_s(t)}{\partial \mathbf{r}_s(t_{0,s})} \right] \right\}^{-1/2} \times \mathcal{C}(t_{0,s}) e^{iS(\tilde{\mathbf{p}}_s, \mathbf{r}_s, t_{0,s}, t)}, \quad (2)$$

where

$$\mathcal{C}(t_{0,s}) = \sqrt{2\pi i / (\partial^2 S(\tilde{\mathbf{p}}_s, \mathbf{r}_s, t_{0,s}, t) / \partial t_{0,s}^2)} \times \langle \mathbf{p}_s(t_{0,s}) + \mathbf{A}(t_{0,s}) | \hat{H}_I(t_{0,s}) | \psi_0 \rangle \quad (3)$$

is a prefactor, $\partial \mathbf{p}_s(t) / \partial \mathbf{r}_s(t_{0,s})$ is related to the stability of the trajectory, and

$$S(\tilde{\mathbf{p}}, \mathbf{r}, t_0, t) = I_p t_0 - \int_{t_0}^t d\tau [\tilde{\mathbf{p}} \cdot \mathbf{r}(\tau) + \tilde{\mathbf{p}}^2/2 + V(\mathbf{r})] \quad (4)$$

denotes the action, where \mathbf{p} is the field-dressed momentum and $\tilde{\mathbf{p}} = \mathbf{p} + \mathbf{A}(\tau)$ with $t_0 < \tau < t$ is the electron velocity. Equation (2) indicates that there are in principle many trajectories along which the electron may be ionized. For the same final momentum, the corresponding transition amplitudes will interfere.

The sum in Eq. (2) is over the semiclassical trajectories starting from position $\mathbf{r}(t_{0,s})$ at time $t_{0,s}$ and ending at momentum $\mathbf{p}(t)$ at time $t \rightarrow \infty$. The index s denotes the different trajectories satisfying three saddle-point equations:

$$[\mathbf{p}_0 + \mathbf{A}(t_0)]^2/2 + I_p = 0, \quad (5)$$

$$\dot{\mathbf{P}}(\tau) = -\nabla_{\mathbf{r}} V[\mathbf{r}(\tau)], \quad (6)$$

and

$$\dot{\mathbf{r}}(\tau) = \mathbf{p}(\tau) + \mathbf{A}(\tau). \quad (7)$$

These equations are solved using an iteration scheme for any given final momentum [10] under the assumption that the electron is ionized by tunneling from t_0 to $t_0^R = \text{Re}[t_0]$ and then reaches the detector at a final (real) time [40,41]. For simplicity, we used $-1/r$ as the form of Coulomb potential for both Ar and N₂ in the simulations. Close to the origin, a regularization procedure was implemented to treat the Coulomb singularities in the complex time plane (See [42] and references therein). The GAMESS code [43] was adopted to calculate the exact wave functions of the $3p$, $m = 0$ state for Ar, neglecting spin orbit interaction and the HOMO of N₂.

IV. RESULTS AND DISCUSSION

In Figs. 2(a) and 2(b) we present the measured photoelectron momentum distributions of Ar and N₂, respectively. One can find distinct fan-shaped interference patterns near the ionization threshold (enclosed by the half circles), i.e., four smaller lobes distributed symmetrically with respect to $p_z = 0$ a.u. for Ar and five lobes with the middle one along $p_z = 0$ a.u. for N₂. For the spiderlike structures, the constructive interferences, i.e., the “spider’s legs” for Ar are analogous with that for N₂. Around $p_z = 0$ a.u., for $0.55 < p_{\perp} < 0.95$ a.u., the carpetlike structures as revealed in previous experiments on Xe [9] can be recognized for both

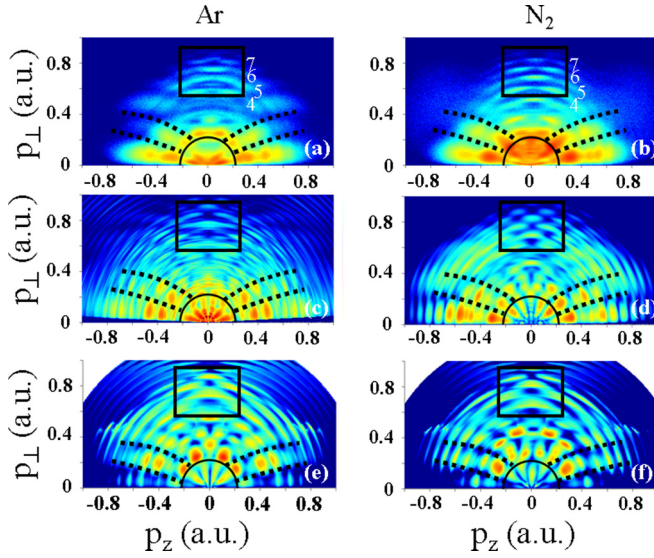


FIG. 2. (a) and (b) Measured photoelectron momentum distributions (in logarithmic scale) from ionization of Ar and randomly aligned N_2 in identical laser fields of a peak intensity of 6.5×10^{13} W/cm², respectively. The laser central wavelength is 788 nm. The abscissa p_z and ordinate $p_{\perp} = \sqrt{p_x^2 + p_y^2}$ denotes the momentum parallel and perpendicular to the laser polarization, respectively. The fan-shaped structures close to the ionization threshold are enclosed by half circles. The minima of the spiderlike structures are indicated with dotted lines. The rectangles mark the carpetlike structures, including several ATI rings along the transverse direction. The numbers represent the orders of ATI rings covered in the rectangles. (c) and (d) TDSE simulations. (e) and (f) CQSFA simulations. To compare with the data, the focal volume effect has been considered in both TDSE and CQSFA simulations. The calculated results for N_2 molecules have been averaged over the random alignment of the internuclear axis. The color scales have been adjusted to highlight the interference structures.

Ar and N_2 (confined by the rectangles). For an intensity of 6.5×10^{13} W/cm², the rectangles cover a number of ATI rings ranging from the fourth to the seventh order. The carpetlike structures clearly exhibit different features for Ar and N_2 . To highlight this discrepancy, we produced a differential hologram by calculating the normalized difference $[D_{\text{Ar}}(\mathbf{p}) - D_{\text{N}_2}(\mathbf{p})]/[D_{\text{Ar}}(\mathbf{p}) + D_{\text{N}_2}(\mathbf{p})]$, where D_{Ar} and D_{N_2} denote the photoelectron distributions for Ar and N_2 , respectively. Here D_{Ar} and D_{N_2} have been normalized to the corresponding maximum photoelectron yield, respectively. The experimental differential hologram is displayed in Fig. 3(a). This hologram reveals that, along $p_z = 0$ a.u., every odd-order (the fifth and seventh orders) ATI rings exhibit minima for Ar but maxima for N_2 . While for every even-order ATI rings (the fourth, sixth, and eighth orders), maxima for Ar but minima for N_2 are observed. In general, when comparing Ar and N_2 , both the fan-shaped and carpetlike interferences are out of phase while the spiderlike interferences are in phase.

The TDSE simulations are shown in Figs. 2(c) and 2(d). Many key features of the experimental results, as described above, are satisfyingly reproduced by our simulations. More lobes for the fan-shaped structures around $p_z = 0$ a.u. in the simulations are not well resolved in the experiments due to

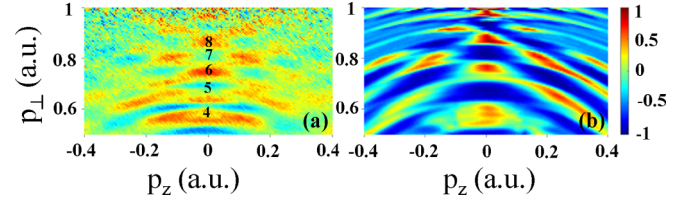


FIG. 3. (a) Blow-up of the experimental normalized momentum difference spectrum between Ar [Fig. 2(a)] and N_2 [Fig. 2(b)]. The numbers represent the orders of ATI rings. (b) The corresponding CQSFA calculation.

the insufficient momentum resolution along the transverse direction.

The CQSFA calculated results shown in Figs. 2(e) and 2(f) agree well with our observations and also the TDSE simulations. The main features of the fan-shaped, spiderlike, and carpetlike structures for Ar and N_2 are faithfully reproduced. The CQSFA underestimates the signal near the polarization axis due to approximations in the continuum propagation [42]. Figure 3(b) displays the calculated differential hologram highlighting the difference of the carpet structures. Again, we find very good agreement between the experiment and simulation. In the CQSFA computations, we consider ionization events only from a finite section of a monochromatic laser field. There will be a fixed starting point, which introduces and effective carrier-envelope phase. This will lead to some left-right asymmetry. We consider ionization events over four cycles, which causes ATI rings. Including more cycles would not affect the position of the rings, only their contrast. The energy region is beyond the direct ATI cutoff $2U_p$ (U_p is the ponderomotive potential). Thus, the carpet is formed by electron trajectories that interact strongly with the core and can only be well reproduced by the interference between types III and IV trajectories within the CQSFA theory (see Fig. 1). Type III orbits have no counterpart in the SFA and behave like field-dressed Kepler hyperbolas, while type IV orbits behave like rescattered SFA trajectories. This is in contrast to previous interpretation based on the SFA theory that the carpet arises from direct electrons [9]. For more details on this specific structure see our recent publication [44].

Encouraged by the overall agreement, we further explore the physical origin of our observations. From Eq. (2) we learn that the interference patterns are closely related to the phase $\text{Re}[S]$, which is accumulated along the pathway starting from the original position, and the prefactor $\mathcal{C}(t_{0,s})$ associated with the atomic or molecular orbital ψ_0 [Eq. (3)]. The stability factor $\partial \mathbf{p}_s(t)/\partial \mathbf{r}_s(t_{0,s})$ is a real term and contains no phase information. In identical laser fields, we find that the difference between phase $\text{Re}[S]$ for different types of trajectory is nearly identical for Ar and N_2 , due to their nearly identical ionization potentials (see Appendix for details). Moreover, the simulations without inclusion of the prefactor $\mathcal{C}(t_{0,s})$ reveal practically identical features for Ar and N_2 (not shown here). Therefore, our observations can be attributed to the different prefactors for Ar and N_2 .

Physically, the prefactor $\mathcal{C}(t_{0,s})$ contains the tunneling probability $\sqrt{2\pi i}/(\partial^2 S(\tilde{\mathbf{p}}_s, \mathbf{r}_s, t_{0,s}, t)/\partial t_{0,s}^2)$ and the tunneling matrix element $\langle \mathbf{p}_s(t_{0,s}) + \mathbf{A}(t_{0,s}) | \hat{H}_I(t_{0,s}) | \psi_0 \rangle$. For each

trajectory type, the phase of the prefactor, i.e., $\Phi_{0,s} = \arg[\mathcal{C}(t_{0,s})]$, is related to the parity of the atomic and molecular orbital. The tunneling probability term has a simple phase that will not be affected by this parity. Here $s = 1, 2, 3$, and 4 correspond to type-I, -II, -III, and -IV trajectories, respectively, as depicted in Fig. 1. In the Appendix, we explain how $\Phi_{0,s}$ leads to the phase differences (or absence thereof) in specific holographic structures. The analysis verifies the physical picture illustrated in Fig. 1: Both the carpetlike and fan-shaped interference structures are sensitive to the parity of the electronic orbital of the target.

V. CONCLUSION

In summary, we show that the parity of atomic and molecular orbitals can be inferred from ultrafast holographic patterns. By using a reference atom and differential measurement, we show that holography patterns such as fan-shaped and carpetlike structures are dephased, while the spiderlike fringes show in phase features when comparing Ar and N₂ with identical laser conditions. Our data are well reproduced by focal- and alignment-averaged time-dependent Schrödinger equation and Coulomb quantum-orbit strong-field approximation (CQSFA) simulations. Using the CQSFA, we trace back the above-mentioned dephasing to parity-related phase differences in the interfering quantum orbits. These phases can be attributed to the different parity of the $3p$ orbital for Ar and the HOMO of N₂.

The method presented in this work is general and can in principle be applied to any holographic pattern in a wide momentum range, for any target or molecular orbital. This may constitute an advantage over more directional methods such as those in [8] and [9], which require restricted momentum ranges. Molecular orbitals other than the HOMO may be probed by scanning alignment angles for which their contributions prevail. This method may also be extended to ultrafast detection of the parity of multielectron wave functions or multiple orbitals, which plays significant roles in more complex molecules [45]. This will be particularly useful for interpreting complex electron dynamics such as charge migration in polyatomic and biological molecules. Finally, one key assumption usually adopted in strong-field ultrafast spectroscopy is that the phase structure of the returning wave packets due to the parity of the initial orbital is smeared out during the propagation [46,47]. However, our joint experimental and theoretical work clearly reveals the parity effects on the interference carpet through rescattering.

The power of this method lies in a choice of known companion or reference atom or molecule to image with. The differences may then inform the features we are interested in measuring. This difference led to parity in the case of Ar and N₂, but it may be used to study other properties. For example, for similar polyatomic molecules, holographic discrepancies could be measured and their source traced back to differences or changes in structure using the trajectories in the CQSFA. Furthermore, one could use isoelectronic homonuclear and heteronuclear molecular pairs, as in [48], with the homonuclear molecule as a reference. This is of great importance for advancing strong-field recollision physics and spectroscopy.

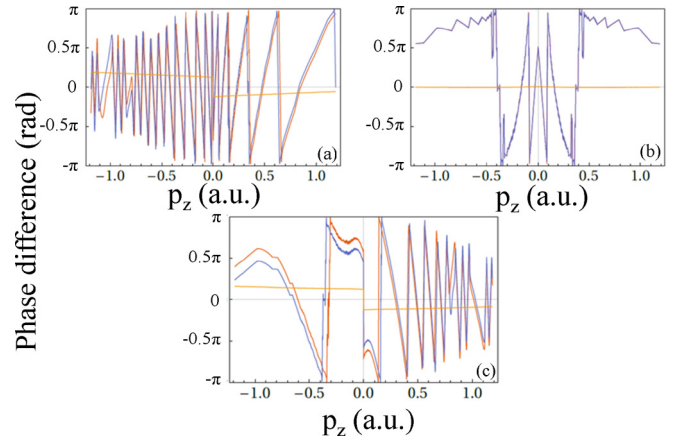


FIG. 4. Calculations for difference between $\text{Re}[S_s]$ for type-II and type-I trajectories (a), between type-III and type-II trajectories (b), and between type-III and type-IV trajectories (c). The red and blue lines represent the results for Ar and N₂, respectively. The orange line in each panel represents the difference between the result of Ar and that of N₂. The abscissa p_z is the final electron momentum along the laser polarization. The final electron momentum perpendicular to the laser polarization p_{\perp} is 0.1 a.u. here. We have found similar features for other values of p_{\perp} . The alignment of N₂ is along the laser polarization axis.

ACKNOWLEDGMENTS

This work is supported by Deutsche Forschungsgemeinschaft. H.P.K. and B.-X.B. are supported by the National Natural Science Foundation of China (Grants No. 11974380, No. 11674363, and No. 91850121). C.F.M.F and A.S.M. acknowledge support from the UK Engineering and Physical Sciences Research Council (EPSRC) (Grants No. EP/J019143/1 and No. EP/P510270/1, respectively). The latter grant is within the remit of the InQuBATE Skills Hub for Quantum Systems Engineering.

APPENDIX

According to the Coulomb quantum-orbit strong-field approximation (CQSFA) theory [14], the phase difference between the involved trajectories plays a crucial role in determining the interference structures. The phase for each trajectory mainly includes two components: the phase obtained along the continuum propagation $\text{Re}[S_s]$ and the phase of the prefactor $\Phi_{0,s}$ relating mainly to the phase of the initial state, which includes the parity of the atomic or molecular orbital. Here $s = 1, 2, 3$, and 4 correspond to type-I, -II, -III, and -IV trajectories, respectively, as explained in our main text. In the following, we will show that, because the ionization potentials of both N₂ and Ar are similar, the phase difference will stem mainly from the prefactor.

1. Phase accumulated along the continuum propagation

Figure 4 shows the calculated phase differences, obtained along the continuum propagation, between different types of trajectories for Ar and N₂. The result for Ar is very similar with that for N₂ in each panel. In Figs. 4(a) and 4(c), there is a small difference between the results of Ar and N₂ (the

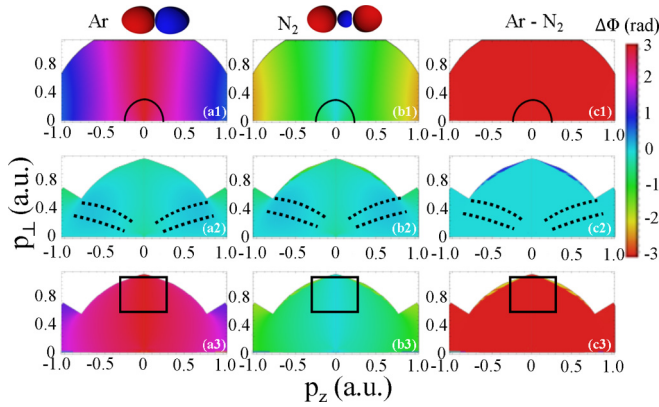


FIG. 5. Calculated diagrams of the difference between $\Phi_{0,s}$ for type-II and type-I trajectories (the first row), between type-III and type-II trajectories (the second row), and between type-III and type-IV trajectories (the third row). The first and second columns show the results for Ar and N_2 , respectively. The differences between the phase diagrams of Ar and N_2 are shown in the third column. The abscissa p_z and ordinate p_{\perp} are the final electron momentum components. The half circles, dotted lines, and rectangles mark the regions where the fan-shaped, spiderlike, and carpetlike structures appear, respectively. The illustrations of the $3p$ orbital for Ar and the highest-occupied molecular orbital (HOMO) of N_2 are shown on the top. The alignment of N_2 is along the laser polarization axis here.

yellow lines), which stems from the fact that the orbits taken into consideration leave from opposite sides. In fact, the phase difference at $p_z = 0$ a.u. is roughly half a cycle times the difference of both ionization potentials. This will be altered slightly as the time difference changes as a function of the parallel momentum. In contrast, for orbits starting on the same

side, this difference is vanishingly small. The fact that these features are subtle can be attributed to the small difference in ionization potentials of Ar (15.76 eV) and N_2 (15.58 eV).

2. Phase of the prefactor

To reveal the influence of the parity of the atomic and molecular orbitals, we calculate the phase of the prefactor $\Phi_{0,s}$ for trajectories leading to the interference patterns of interest. Then we obtain the difference between $\Phi_{0,s}$ for the trajectories responsible for each interference pattern, as shown in Fig. 5. For Ar, there is an additional $\sim\pi$ difference between $\Phi_{0,s}$ for type-II and type-I trajectories in the electron momentum region where the fan-shaped structures appear [Fig. 5(a1)], while this additional phase difference is around 0 for N_2 [Fig. 5(b1)]. This is due to the different parities of $3p$ orbital for Ar and the HOMO of N_2 , since type-II and type-I trajectories arise from the opposite sides of the target. Figure 5(c1) shows the difference between Fig. 5(a1) and Fig. 5(b1). Now all other phases cancel, which clearly reveals a π shift between the phase diagram of Ar and N_2 . The same π phase shift can be found for the carpetlike interference (third row of Fig. 5), where the trajectories type-III and type-IV tunnel exits lie on opposite sides of the target. For the region where the spiderlike interference shows up, the phase difference is basically the same for Ar and N_2 [Figs. 5(a2) and 5(b2)] because type-II and type-III trajectories are released from the same side of the target. There is thus no phase shift between the phase diagram of Ar and N_2 [Figs. 5(c2)]. Note that the internuclear axis of N_2 is aligned along the laser polarization axis in the above computation. The ionization probability for N_2 is maximal for this alignment angle and decreases fast for other alignment angles [49]. Thus, we expect that this also holds true for randomly distributed alignments of N_2 in our experiments.

- [1] T. D. Lee and C. N. Yang, *Phys. Rev.* **104**, 254 (1956).
- [2] R. R. Freeman, P. H. Bucksbaum, H. Milchberg, S. Darack, D. Schumacher, and M. E. Geusic, *Phys. Rev. Lett.* **59**, 1092 (1987).
- [3] J. Muth-Böhm, A. Becker, and F. H. M. Faisal, *Phys. Rev. Lett.* **85**, 2280 (2000).
- [4] M. Meckel, D. Comtois, D. Zeidler, A. Staudte, D. Pavičić, H. C. Bandulet, H. Pépin, J. C. Kieffer, R. Dörner, D. M. Villeneuve, and P. B. Corkum, *Science* **320**, 1478 (2008).
- [5] M. Meckel, A. Staudte, S. Patchkovskii, D. M. Villeneuve, P. B. Corkum, R. Dörner, and M. Spanner, *Nat. Phys.* **10**, 594 (2014).
- [6] M. M. Liu, M. Li, C. Wu, Q. Gong, A. Staudte, and Y. Liu, *Phys. Rev. Lett.* **116**, 163004 (2016).
- [7] M. Kunitski, N. Eicke, P. Huber, J. Köhler, S. Zeller, J. Voigtsberger, N. Schlott, K. Henrichs, H. Sann, F. Trinter, L. Ph. H. Schmidt, A. Kalinin, M. S. Schöffler, T. Jahnke, M. Lein, and R. Dörner, *Nat. Commun.* **10**, 1 (2019).
- [8] X. Xie, S. Roither, D. Kartashov, E. Persson, D. G. Arbó, L. Zhang, S. Gräfe, M. S. Schöffler, J. Burgdörfer, A. Baltuška, and M. Kitzler, *Phys. Rev. Lett.* **108**, 193004 (2012).
- [9] Ph. A. Korneev, S. V. Popruzhenko, S. P. Goreslavski, T.-M. Yan, D. Bauer, W. Becker, M. Kübel, M. F. Kling, C. Rödel, M. Wünsche, and G. G. Paulus, *Phys. Rev. Lett.* **108**, 223601 (2012).
- [10] X. Y. Lai, C. Poli, H. Schomerus, and C. Figueira de Morisson Faria, *Phys. Rev. A* **92**, 043407 (2015).
- [11] A. S. Maxwell, A. Al-Jawahiry, T. Das, and C. Figueira de Morisson Faria, *Phys. Rev. A* **96**, 023420 (2017).
- [12] A. S. Maxwell and C. Figueira de Morisson Faria, *J. Phys. B* **51**, 124001 (2018).
- [13] Y. Huismans *et al.*, *Science* **331**, 61 (2011).
- [14] C. Figueira de Morisson Faria and A. S. Maxwell, *Rep. Prog. Phys.* **83**, 034401 (2020).
- [15] P. B. Corkum, *Phys. Rev. Lett.* **71**, 1994 (1993).
- [16] Y. Zhou, O. I. Tolstikhin, and T. Morishita, *Phys. Rev. Lett.* **116**, 173001 (2016).
- [17] M. He, Y. Li, Y. Zhou, M. Li, W. Cao, and P. Lu, *Phys. Rev. Lett.* **120**, 133204 (2018).
- [18] S. Walt, N. Ram, M. Atala, N. Shvetsov-Shilovski, A. von Conta, D. Baykusheva, M. Lein, and H. Wörner, *Nat. Commun.* **8**, 15651 (2017).
- [19] A. Rudenko *et al.*, *J. Phys. B* **37**, L407 (2004).
- [20] C. M. Maharjan *et al.*, *J. Phys. B* **39**, 1955 (2006).
- [21] T. Marchenko, H. G. Muller, K. J. Schafer, and M. J. J. Vrakking, *J. Phys. B* **43**, 095601 (2010).

- [22] D. G. Arbó, S. Yoshida, E. Persson, K. I. Dimitriou, and J. Burgdörfer, *Phys. Rev. Lett.* **96**, 143003 (2006).
- [23] Z. Chen, T. Morishita, A.-T. Le, M. Wickenhauser, X. M. Tong, and C. D. Lin, *Phys. Rev. A* **74**, 053405 (2006).
- [24] D. G. Arbó, K. I. Dimitriou, E. Persson, and J. Burgdörfer, *Phys. Rev. A* **78**, 013406 (2008).
- [25] T.-M. Yan, S. V. Popruzhenko, M. J. J. Vrakking, and D. Bauer, *Phys. Rev. Lett.* **105**, 253002 (2010).
- [26] Y. Deng, Y. Liu, X. Liu, H. Liu, Y. Yang, C. Wu, and Q. Gong, *Phys. Rev. A* **84**, 065405 (2011).
- [27] X. Y. Lai, S. G. Yu, Y. Y. Huang, L. Q. Hua, C. Gong, W. Quan, C. F. Faria, and X. J. Liu, *Phys. Rev. A* **96**, 013414 (2017).
- [28] A. S. Maxwell, A. Al-Jawahiry, X. Y. Lai, and C. Figueira de Morisson Faria, *J. Phys. B* **51**, 044004 (2018).
- [29] J. Ullrich, R. Moshhammer, A. Dorn, R. Dörner, L. P. H. Schmidt, and H. Schmidt-Böcking, *Rep. Prog. Phys.* **66**, 1463 (2003).
- [30] A. S. Alnaser, X. M. Tong, T. Osipov, S. Voss, C. M. Maharjan, B. Shan, Z. Chang, and C. L. Cocke, *Phys. Rev. A* **70**, 023413 (2004).
- [31] O. Jagutzki, A. Cerezo, A. Czasch, R. Dörner, M. Hattas, M. Huang, V. Mergel, U. Spillmann, K. Ullmann-Pfleger, T. Weber, H. Schmidt-Böcking, and G. D. W. Smith, *IEEE Trans. Nucl. Sci.* **49**, 2477 (2002).
- [32] X. B. Bian, Y. Huisman, O. Smirnova, K. J. Yuan, M. J. J. Vrakking, and A. D. Bandrauk, *Phys. Rev. A* **84**, 043420 (2011).
- [33] X. B. Bian and A. D. Bandrauk, *Phys. Rev. A* **89**, 033423 (2014).
- [34] X. M. Tong and C. D. Lin, *J. Phys. B* **38**, 2593 (2005).
- [35] V. I. Usachenko and S.-I. Chu, *Phys. Rev. A* **71**, 063410 (2005).
- [36] H. Kleinert, *Path Integrals in Quantum Mechanics, Statistics, Polymer Physics, and Financial Markets* (World Scientific, Singapore, 2009).
- [37] D. B. Milošević, *J. Math. Phys.* **54**, 042101 (2013).
- [38] R. Kopold, W. Becker, and M. Kleber, *Opt. Commun.* **179**, 39 (2000).
- [39] C. F. M. Faria, H. Schomerus, and W. Becker, *Phys. Rev. A* **66**, 043413 (2002).
- [40] S. V. Popruzhenko and D. Bauer, *J. Mod. Opt.* **55**, 2573 (2008).
- [41] S. V. Popruzhenko, *J. Phys. B* **47**, 204001 (2014).
- [42] A. S. Maxwell, S. V. Popruzhenko, and C. F. M. Faria, *Phys. Rev. A* **98**, 063423 (2018).
- [43] M. W. Schmidt *et al.*, *J. Comput. Chem.* **14**, 1347 (1993).
- [44] A. S. Maxwell, X.-Y. Lai, R. Sun, X. Liu, and C. F. M. Faria, *arXiv:2003.02239*.
- [45] H. Akagi, T. Otobe, A. Staudte, A. Shiner, F. Turner, R. Dörner, D. M. Villeneuve, and P. B. Corkum, *Science* **325**, 1364 (2009).
- [46] J. Itatani, J. Levesque, D. Zeidler, H. Niikura, H. Pépin, J. C. Kieffer, P. B. Corkum, and D. M. Villeneuve, *Nature (London)* **432**, 867 (2004).
- [47] O. Smirnova and M. Y. Ivanov, in *Attosecond and XUV Spectroscopy: Ultrafast Dynamics and Spectroscopy*, edited by T. Schultz and M. J. J. Vrakking (Wiley, New York, 2014), pp. 201–256.
- [48] B. B. Augstein and C. F. M. Faria, *J. Phys. B* **44**, 055601 (2011).
- [49] H. Kang, W. Quan, Y. Wang, Z. Lin, M. Wu, H. Liu, X. Liu, B. B. Wang, H. J. Liu, Y. Q. Gu, X. Y. Jia, J. Liu, J. Chen, and Y. Cheng, *Phys. Rev. Lett.* **104**, 203001 (2010).